Bi-instability as a precursor to global mixed-mode chaos

Ira B. Schwartz

Special Project in Nonlinear Science, Naval Research Laboratory, Code 6700.3, PPD, Washington, D.C. 20375

Thomas W. Carr

Department of Mathematics, Southern Methodist University, Dallas, Texas 75275-0156

(Received 14 September 1998)

Bi-instability, in contrast to bistability, is shown to generate unstable chaotic saddles prior to the onset of chaos. The theory and numerics are applied to a CO_2 laser model with modulated losses where unstable pairs of saddles coexist, form heteroclinic connections, and allow mixing between local chaotic attractors to produce global mixed-mode chaos. [S1063-651X(99)09906-7]

PACS number(s): 05.45.−a

One of the major areas of research and testbeds of nonlinear dynamics has been that of lasers [1]. Common to many types of lasers that undergo bifurcations to chaos are optical bistability and hysteresis. Bistability results from the existence of nonlinear interactions between the electromagnetic field and population inversion, or gain. In most cases, bistability, or generalized multistability, is associated indirectly with the onset of chaos. This can be seen in examples such as coupled chaotic class-B lasers [2], modulated class-B lasers [3,4], and fiber lasers [5]. Bistability and chaos also appear in other fields, such as subharmonic bifurcation in population biology [6], chemical kinetics [7], and neurophysiology [8], to name just a few. An outstanding problem in many of these fields is the recognition and understanding of the role of unstable orbits in connecting bistability to chaos. The thesis of the current letter is that *bi-instability*, in contrast to *bistability*, is the precursor to global chaos that has two fundamental frequency components formed by the merging of two basins of attraction. We define chaos, which has two fundamental frequency components, as global mixed-mode chaos. Global mixed-mode chaos is observed experimentally and theoretically in a wide class of problems describing the dynamics of systems involving large populations, including laser and chemical dynamics such as those listed above.

Analytical methods to show the existence of chaos prove the existence of transverse crossings of manifolds emanating from unstable periodic orbits. In general, there are very few methods to carry out this procedure. One example is Melnikov's method, but the drawback is that the conservative system must possess certain symmetry requirements [9]. Furthermore, the responsible unstable orbits may not be related to perturbations of a conservative system [10,11]. On the other hand, numerical location and tracking of manifolds have progressed to where it is now practical to implement on a computer [12]. To illustrate the origin of global mixed-mode chaos, we show the coexistence of two unstable orbits of different frequencies in the modulated CO_2 laser. Their respective manifolds are tracked numerically and form a heteroclinic connection, which is the origin of a chaotic saddle (also an unstable dynamical object). The chaotic saddle can form only in the presence of two unstable periodic orbits, and it appears immediately after the two saddles coexist. We conjecture that the heteroclinic connection is the source of observed mixed-mode chaos.

To illustrate the topological ideas of global mixed-mode chaos, we consider the scaled equations for a single-mode periodically modulated class-B laser [3,10,13]:

$$x' = -y - \epsilon x(a+by),$$
$$y' = (1+y)(x - \delta \cos(\omega t)), \tag{1}$$

where x is the population inversion, y the intensity, ϵ the dissipation parameter, a and b are related to the pump, and δ and ω are the forcing amplitude and frequency [14]. For $\delta < 1.57$ the system exhibits small-amplitude period-1 SA-$P(1)$ based chaos; the small-amplitude oscillations in Fig. 1 are transient vestiges of the $P(1)$ chaos. Coexisting with the SA-$P(1)$ chaos basin is a large-amplitude period-2 LA-$P(2)$ orbit. [The SA-$P(1)$ basin and LA-$P(2)$ basins are shown by the light and dark gray regions of Fig. 3, re-
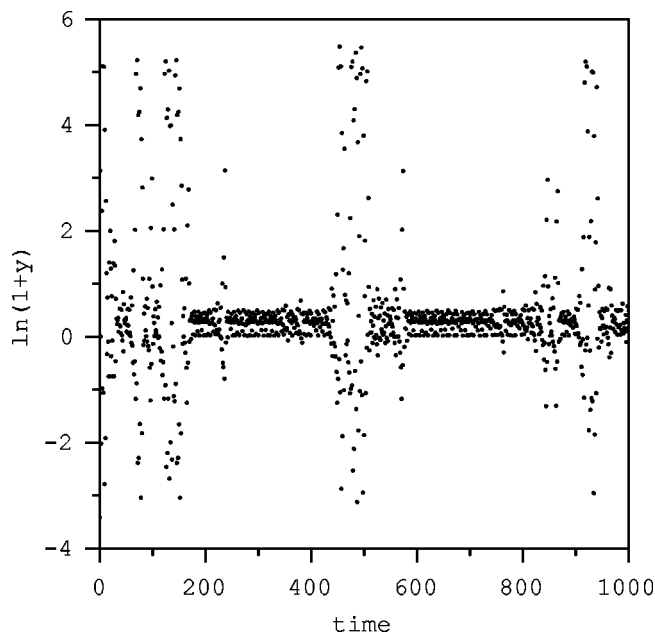

FIG. 1. For $\delta = 1.57$, discrete-time series of trajectory showing bursts from SA-$P(1)$ into the LA-$P(2)$ basin. This and all later numerical computations use $\omega = 0.9$, $\epsilon = 0.001$, $a = 56.0$, and $b = 3.0$

spectively]. At $\delta = 1.57$ the system asymptotes to a large-amplitude period-4 orbit in the LA-$P(2)$ basin after displaying the bursting transients shown in Fig. 1. The bursts are $P(2)$ based, while the small amplitude chaos is $P(1)$ based. Since the spectrum contains two dominant frequency components, the transient is a global mixed-mode chaotic transient. For higher δ, attracting chaos develops in the LA-$P(2)$ basin. This is followed by *global* mixed-mode chaos where the chaotic trajectory visits both regions of phase space previously defined by the separated basins and has $P(1)$ and $P(2)$ dominant spectral components.

Bi-instability onset is seen by following the approach of Schwartz and Erneux (SE) [13] to construct a map describing the pulsating solutions. While SE [13] considered the conservative laser, our map will include the effects of dissipation when $\epsilon \neq 0$. Newell *et al.* [15] also used the matched asymptotics approach to derive a map for the two-frequency modulation of a fiber laser that included the effects of dissipation. However, their map did not allow for easy analytical investigation, and was used for numerical simulation only. As the details of the map construction were discussed in both Refs. [13,14], we show only the result (details will be presented in a future publication)

$$t_{n+1} = t_n - 2x_n - \tfrac{2}{3}\gamma x_n^2, \tag{2a}$$

$$x_{n+1} = x_n + \tfrac{2}{3}\gamma x_n^2 + 2\delta \cos(\omega t_{n+1}), \tag{2b}$$

where $\gamma = \epsilon(a - b)$. The variables t_n and x_n specify the time (t_n) where the population x reaches its minimum x_n. Hence $t_{n+1} - t_n$ corresponds to the period of the oscillations.

Fixed-point solutions to Eqs. (2) occur when x_n and the difference $t_{n+1} - t_n$ is constant. Primary saddle and node solutions are single loop orbits of the form $x_{n+1} = x_n = x_f$ and $t_{n+1} - t_n = P(m), P(m) = 2\pi m/\omega, m = 1,2,3, \dots$. With these conditions and substituting into Eq. (2a) we obtain $\tfrac{2}{3}\gamma x_f^2 + 2x_f + P(m) = 0$. Real values of x_f require that $P(m) \leq 3/2\gamma$; thus dissipation limits the maximum period of subharmonic solutions. Of the two solutions for x_f one is singular as $\gamma \to 0$ but does not appear until $\delta = O(1/\gamma)$. We will focus on the regular solution that in the limit $\gamma \to 0$ reduces to the result of SE [13]:

$$x_f = \frac{-P(m)}{2} - \frac{\gamma}{12}P(m)^2 + O(\gamma^2). \tag{3}$$

A second existence condition comes from Eq. (2b), where we use that $|\cos(\omega t_f)| \leq 1$; this requires $(\gamma/3\delta)x_f^2 \leq 1$. Equation (3) is substituted for x_f to obtain a relationship between the forcing and the period of the subharmonic orbit given by

$$\delta \geq \delta_{SN} = \frac{\gamma}{12}P(m)^2 + O(\gamma^2). \tag{4}$$

where δ_{SN} defines the primary saddle-node (SN) bifurcation (PSNB) point. A similar condition was derived by Schwartz in Ref. [10], but here we are able to specify the condition explicitly in terms of the physical parameters.

For a single value of x_f there are two possible values of t_f differentiated by $\sin(\omega t_f) > 0 (<0)$. Linear stability shows that these correspond to the saddle and node solutions, respec-
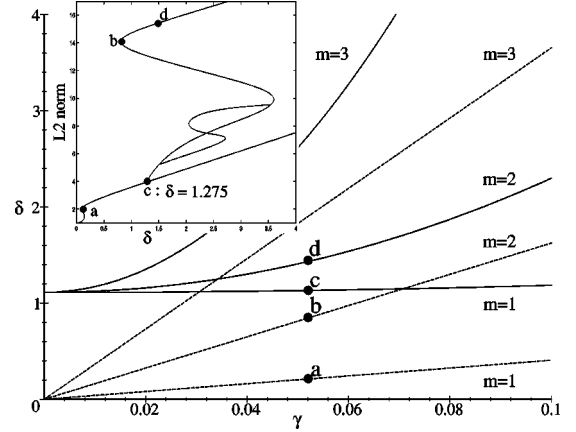

FIG. 2. For a given γ, dotted curves indicate the value of δ_{SN} for period $P(m), m = 1$, 2, and 3. Solid curves indicate the value of δ_{PD}. The inset is the corresponding bifurcation diagram for the $L2$ norm of Eq. (1).

tively. The linear stability of these solutions can be examined by substituting $x_n = x_f + X_n, t_n = t_f + nP(m) + T_n$ into Eqs. (2) and considering X_n and T_n small. The $P(m)$ node solution is found to undergo a flip bifurcation, corresponding to period-doubling bifurcation in Eq. (1), when

$$\delta_{PD} = \frac{1}{\omega} + \gamma^2 \frac{\omega}{288}P(m)^4. \tag{5}$$

The resulting period-doubled (PD) solutions are defined as $x_{n+2} = x_n, t_{n+2} - t_n = P(m)$. For $\gamma \ll 1$ the bifurcation equation is $\delta = \delta_{PD} + (\omega/6)(x - x_f)^2$.

Equations (4) and (5), shown in Fig. 2, provide a template for understanding the organization of the PSNB and PD bifurcations; the map results agree qualitatively with numerical bifurcation diagram of (1) shown inset. When $\gamma = 0.053$ and the forcing δ is increased, the laser's bifurcation sequence is the following: (a) $P(1)$-PSNB, (b) $P(2)$-PSNB, (c) PD bifurcation of the $P(1)$ node solution, (d) and PD bifurcation of the $P(2)$ node solution.

Based on the bifurcation analysis in Fig. 2, we examine the dynamics before and after the onset of bi-instability. We define $\delta = \delta_{bi} = 1.275$ as that value corresponding to point (c), the ''PD bifurcation of the $P(1)$-node solution.'' For $\delta < \delta_{bi}$ the $P(2)$ saddle is the only unstable orbit. For $\delta > \delta_{bi}$ there is the addition of the $P(1)$-flip saddle. The coexistence of the $P(2)$-regular saddle and the $P(1)$-flip saddle determines a region of bi-instability.

In Fig. 3 we examine the bi-instability just after onset when $\delta = 1.3$. The dark gray region corresponds to the basin of attraction for the LA-$P(2)$-node orbit. The light gray region corresponds to the SA-$P(2)$-PD orbit produced by the flip bifurcation at $\delta = \delta_{bi}$. In addition to the basins of attraction, a picture of a chaotic saddle was computed using the saddle-straddle procedure described in Ref. [12]. It is observed that points on the chaotic saddle asymptote to the SA-$P(2)$-flip saddle. This means that the stable manifold of the SA-$P(2)$-flip saddle is contained in the chaotic saddle.

Before showing which manifolds are explicitly involved in the creation of the chaotic saddle, we remark that for values of $\delta < \delta_{bi}$, the basins of attraction for the $P(2)$- and
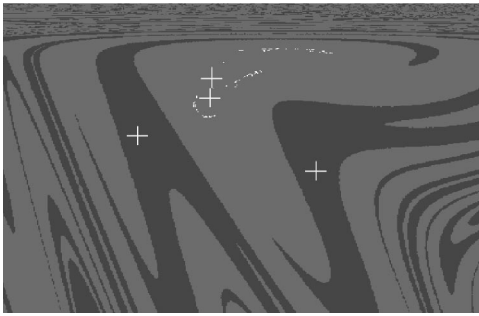
FIG. 3. Attractor basins or SN period-2 orbits (dark) and PD period-2 orbits (light) for $\delta = 1.3$. The chaotic saddle is also shown in white. See Fig. 4 for other figure details.

$P(1)$-node orbits look similar to that of Fig. 3, but with one major difference. Even though the situation is bistable, there are no chaotic saddles or unstable objects which can produce any crossings of manifolds. We reiterate that *bistability alone cannot be responsible for the appearance of any chaotic dynamics.*

Figures 4 and 5 are period-2 Poincaré maps that show the manifolds of the saddle orbits before and after $\delta = \delta_{bi}$. The LA-$P(2)$ saddle and its image after one period are overlaid with the arrows. From Figs. 3–5, we see that the stable manifolds of the LA-$P(2)$ saddle define the basin boundary. Specifically, in Fig. 4 for $\delta < \delta_{bi}$, the left unstable manifold of the LA-$P(2)$ saddle spirals to the stable LA-$P(2)$ node (similarly for the ''images''). The right unstable manifold spirals in a complicated way to the stable SA-$P(1)$ node.

Figure 5 shows the situation when $\delta > \delta_{bi}$ (after the PD bifurcation). The two new $+$ signs in the center show the new SA-$P(2)$-PD orbit and its image, resulting from the PD bifurcation of the SA-$P(1)$ node. The new manifold is the *stable* manifold of the new SA-$P(1)$-flip saddle. A heteroclinic connection is formed by the intersection of this stable manifold with the *unstable* manifold of the LA-$P(2)$ saddle. The intersection points of these manifolds determine the chaotic saddle shown by the white points in Fig. 3.

As the forcing is increased, the dynamics become much more complicated; Fig. 6 shows the manifolds for $\delta = 1.57$.
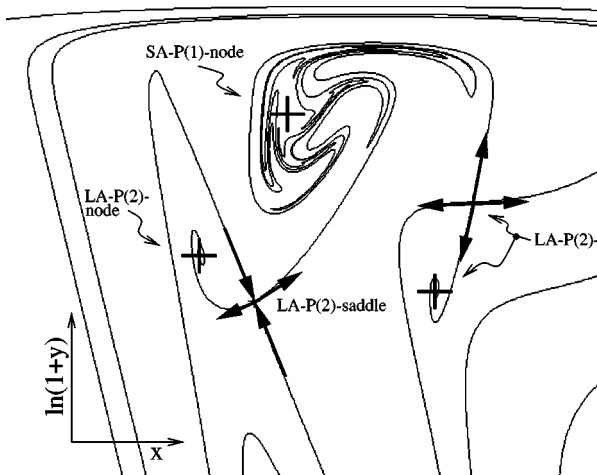

FIG. 5. For $\delta = 1.3$ coexistence of the LA-$P(2)$-node solution and the SA-$P(2)$-PD solution from the period-1 branch. ''Images'' of SA-$P(2)$ are shown only with $+$. The axis and ranges are the same as those of Fig. 4.

The LA-$P(2)$ saddle is the same. However, now the SA-$P(1)$-flip saddle and its *unstable* manifold are depicted [contrast to Fig. 5 where the the SA-$P(2)$-PD orbit and SA-$P(1)$-flip saddle's stable manifold are depicted].

The square highlights a homoclinic intersection of the LA-$P(2)$ saddle's stable and unstable manifolds; similar intersections exist but are not shown for the SA-$P(1)$-flip saddle. Thus homoclinic intersections influence the dynamics local to any $P(m)$-node orbit and its subsequent period-doubled orbits. However, the global dynamics are controlled by heteroclinic interactions. The circle highlights the reverse-heteroclinic connection of the SA-$P(1)$-flip saddle's *unstable* manifold with the LA-$P(2)$-saddle's *stable* manifold. This corresponds to the injection of trajectories into the LA-$P(2)$ basin. *The bursting seen in the discrete time-series of Fig. 1 results from the reverse-heteroclinic intersection.*

We now summarize the sequence of bifurcations and connections. A forward-heteroclinic intersection forms immediately at the onset of bi-instability, $\delta = \delta_{bi}$, between a

FIG. 4. For $\delta = 1.0$ coexistence of LA-$P(2)$-node solution and SA-$P(1)$-node solution. The windows shown are $x \in (-10,10)$ and $\ln(1+y) \in (-29,6)$.
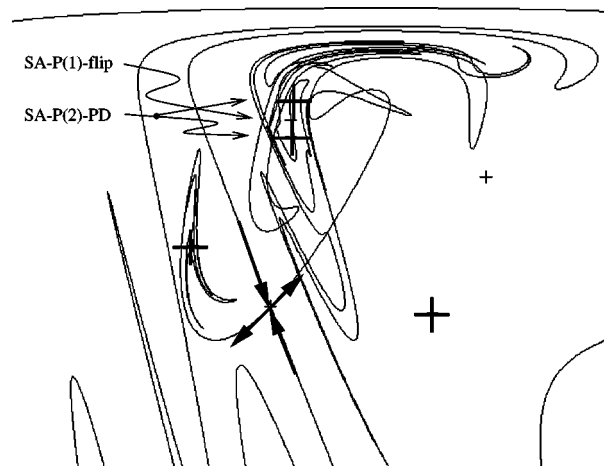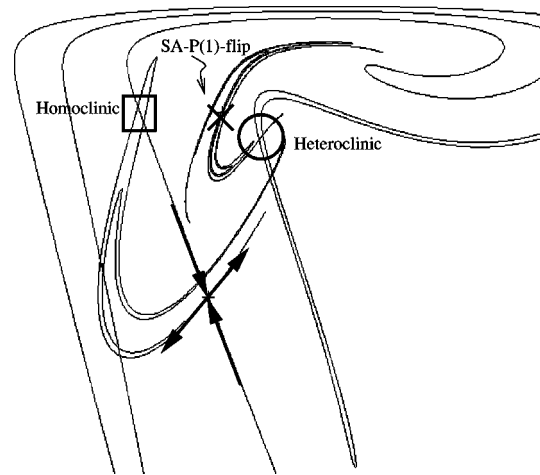

FIG. 6. For $\delta = 1.57$, homoclinic intersections (boxed) for the LA-$P(2)$ saddle and the reverse-heteroclinic intersection between the SA-$P(1)$ and LA-$P(2)$ saddles (circled). The axis and ranges are the same as those of Fig. 4.

period-2 regular saddle and a period-1 flip saddle. The forward heteroclinic intersection is responsible for a chaotic saddle resulting in complex transient phenomena in the SA-$P(1)$ basin of attraction. For a larger value of the forcing, a reverse-heteroclinic intersection is created. This again leads to complex transient phenomena as the trajectory is injected into the LA-$P(2)$ basin.

For $\delta = 1.57$ the bursting transient eventually decays to a period-4 orbit created by a PD bifurcation of the LA-$P(2)$ node. As δ is increased, a period-doubling route to chaos develops due to homoclinic intersections within this basin. As the chaotic attractor grows there is an internal crisis such that some trajectories are injected back into the SA-$P(1)$ basin. This leads to sustained bursting as the preexisting reverse-heteroclinic connection sends trajectories back out of the SA-$P(1)$ basin. The basins are now connected such that a spectral analysis of the resulting chaos has two dominant centers based on the original SA-$P(1)$ and LA-$P(2)$ saddles.

Localized chaos (restricted in phase space) develops in both the SA-$P(1)$ basin and the LA-$P(2)$ basin due to homoclinic intersections. However, global mixed-mode chaos such that the dynamics visits regions of phase space previously delineated by these basins results from the existence of two saddles or bi-instability. The reverse-heteroclinic inter-section corresponds to a crisis event that sends the dynamics into the LA-$P(2)$ regime. As the LA-$P(2)$-based chaotic attractor grows in collides with the original LA-$P(2)$ saddle; this crisis event sends trajectories back to the original SA-$P(1)$ regime [11] directed by the forward-heteroclinic connection. The resulting highly mixed dynamics is what we referred to as ''global chaos'' and as described in the introduction such dynamics is seen both in numerics and experiments in a variety of applications.

The analysis done was in the neighborhood of a PD bifurcation point. This suggests that the chaotic saddle may be observed in a prechaotic parameter range experimentally by observing the transient dynamics in a region near a PD operating point.

Finally, Eqs. (2) are useful to understand the organization of the SN and PD bifurcations and will be explored further in a later report. The well-known Ikeda map [12] was derived for a passive optical cavity. This contrasts Eqs. (2), which are derived for an active-laser cavity.

---

[1] N.B. Abraham, P. Mandel, and L.M. Narducci, Prog. Opt. **25**, 3 (1988); L.M. Narducci and N.B. Abraham, *Laser Physics and Laser Instabilities* (World Scientific, Singapore, 1988).

[2] K.S. Thornburg, M. Moller, R. Roy, T.W. Carr, R.D. Li, and T. Erneux, Phys. Rev. E **55**, 3865 (1997); A.I. Khubnik, Y. Braiman, T.A.B. Kennedy, and K. Wiesenfeld, Physica D **111**, 295 (1998).

[3] F.T. Arrecchi, G.L. Lippi, G.P. Puccioni, and J.R. Tredicce, Opt. Commun. **51**, 308 (1984).

[4] V.N. Chizhevsky and R. Corbaln, Phys. Rev. E **54**, 4576 (1996); H.G. Solari, E. Eschenazi, R. Gilmore, and J.R. Tredicce, Opt. Commun. **64**, 49 (1987); J.R. Tredicce, F.T. Arecchi, G.P. Puccioni, A. Poggi, and W. Gadomski, Phys. Rev. A **34**, 2073 (1986); F. Papoff, D. Dangoisse, E. Poite-Hanoteau, and P. Glorieux, Opt. Commun. **67**, 358 (1988); D. Dangoisse, P. Glorieux, and D. Hennequin, Phys. Rev. A **36**, 4775 (1987); F.T. Arrecchi, G.L. Lippi, G.P. Puccioni, and J.R. Tredicce, Opt. Commun. **51**, 308 (1988).

[5] D. Dangoisse, J.-C. Celet, and P. Glorieux, Phys. Rev. E **56**, 1396 (1997).

[6] I.B. Schwartz, and H.A. Smith, J. Math. Biol. **18**, 223 (1983).

[7] I. R. Epstein and J. A. Pojman, *An Introduction to Nonlinear Chemical Dynamics* (Oxford University Press, New York, 1998).

[8] F. Pasemann, Physica D **104**, 205 (1997).

[9] M. Taki, Phys. Rev. E **56**, 6033 (1997).

[10] T. Erneux, S.M. Baer, and P. Mandel, Phys. Rev. A **35**, 1165 (1987); I.B. Schwartz, Phys. Lett. A **126**, 411 (1988).

[11] I.B. Schwartz, Phys. Rev. Lett. **60**, 1359 (1988).

[12] H.E. Nusse and J.A. Yorke, Physica D **36**, 189 (1989).

[13] I.B. Schwartz and T. Erneux, SIAM (Soc. Ind. Appl. Math.) J. Appl. Math. **54**, 1083 (1994).

[14] Although the analysis presented concentrates on period-2 subharmonics, the model has been used to predict up to period-11 subharmonics which have been observed in experiments. See R. Gilmore, Rev. Mod. Phys. **70**, 1455 (1998), and the references cited within.

[15] T.C. Newell, A. Gavrielides, V. Kovanis, D. Sukow, T. Erneux, and S.A. Glasgow, Phys. Rev. E **56**, 7223 (1997).